A&A 435, 1123–1135 (2005)
DOI: 10.1051/0004-6361:20042169

Astronomy & Astrophysics

A model of the Alfvén speed in the solar corona

A. Warmuth and G. Mann

Astrophysikalisches Institut Potsdam, An der Sternwarte 16, 14482 Potsdam, Germany
e-mail: awarmuth@aip.de

Received 13 October 2004 / Accepted 28 January 2005

Abstract. We present an analytic model of the Alfvén speed v_A in the solar corona. The coronal magnetic field is modeled by a radial component representing the global field and by a dipole representing an active region. The free parameters of the model are constrained by actual observations of solar magnetic fields and coronal electron densities. The coronal magnetic field strength in the quiet Sun is determined by coronal seismology, using EIT waves as proxies for the fast magnetosonic speed v_{ms}, and thus for the magnetic field strength. Depending on the orientation of the dipole, we find local minima of v_A (and v_{ms}) at the coronal base at distances of 0.2–0.3 solar radii from the center of the modelled active region (AR), as well as above the AR at comparable heights. For all dipole orientations, a global maximum is found at 3.5 solar radii. We apply our model to the study of the formation and propagation of coronal shock waves which are observed as flare waves and as type II radio bursts, using a sample of eight solar events. We find that flare waves are initially highly supermagnetosonic (with magnetosonic Mach numbers of $M_{ms} \approx 2$–3). During their propagation, they decelerate until $M_{ms} = 1$ is reached. This behavior can be explained by a strong shock or large-amplitude simple wave that decays to an ordinary fast magnetosonic wave. The observed starting frequencies and Mach numbers of the associated type II bursts are consistent with the predictions of the model.

Key words. Sun: corona – Sun: magnetic fields – Sun: radio radiation – shock waves

1. Introduction

Eruptive phenonmena play an important role during active processes at the Sun. For instance, they appear as jets (e.g. Brueckner & Bartoe 1983) associated with the magnetic reconnection process, Moreton waves (Moreton & Ramsey 1960) seen in Hα, coronal transient waves (also called EIT waves) observed in the EUV range (Moses et al. 1997; Thompson et al. 1998), coronal mass ejections (CMEs; see e.g. Harrison 1986, for a review) and shocks (Uchida 1968; Wagner & MacQueen 1983; Aurass 1996). In the solar corona, shock waves can immediately be generated by the flare process as blast waves (Uchida et al. 1973; Vršnak et al. 1995) and/or appear as bow shocks driven by CMEs (Stewart et al. 1974a,b). They can continue into interplanetary space. Coronal and interplanetary shocks can be source of type II radio bursts (Wild & McCready 1950; Uchida 1960; Cane et al. 1981). Since shock waves are able to accelerate particles, they are potential sources of solar energetic particles (SEPs; Cane et al. 1981; Cairns & Robinson 1987; Mann & Klassen 2002). Especially, the CME-driven interplanetary shocks are generally regarded as the source of the long-living SEPs (e.g. Kahler 1994; Reames et al. 1996).

For the understanding of the formation and development of these phenomena the knowledge of the behaviour of the Alfvén speed in the solar corona and near-Sun interplanetary space is of great importance, since it is the most important characteristic speed in a magneto-plasma (see e.g. Priest 1982). For instance, in a magnetized plasma a fast magnetosonic shock wave is formed if the velocity of the disturbance excedes the local fast magnetosonic speed. Furthermore, EIT waves are considered as a manifestation of a fast magnetosonic wave travelling over the whole hemisphere in the low corona (Mann et al. 1999a).

Mann et al. (2003, henceforth Paper I) studied the formation and development of shock waves in the solar corona and near-Sun interplanetary space by evaluating the behaviour of the local Alfvén speed along a straight path away from an active region. This requires a model of the magnetic field of an active region superimposed on that of the quiet Sun and a density model. Since the behaviour of the Alfvén speed is very important for understanding different phenomena at the active Sun, we intend to revisit this subject in the present paper. We compute the various coronal parameters (e.g. the Alfvén speed), not only along a straight trajectory as was done in Paper I, but in the whole corona and near-Sun interplanetary space. Here, the magnetic field of an active region is modelled by a magnetic dipole, with different orientations of the dipole axis. In addition, we include a density enhancement in the active region.

The model is described in Sect. 2, while in Sect. 3, the free parameters of the model are constrained by using magnetographic observations as well as published electron density measurements. In Sect. 4, we discuss the computed coronal parameters and their distribution. We then study the propagation of flare waves and type II radio bursts using the computed coronal parameters. The conclusion is given in Sect. 5.

2. The coronal magnetic field model

The study of the formation and evolution of large-scale MHD waves and shocks requires the knowledge of the characteristic velocities in the corona. The Alfvén speed is usually defined as

$$v_\mathrm{A} = \frac{B}{\sqrt{4\pi\mu_0\bar{\mu}m_\mathrm{p}n}}, \tag{1}$$

where B is the magnetic field strength, μ_0 the magnetic permeability of vacuum, $\bar{\mu}$ the mean molecular weight (taken as $\bar{\mu} = 0.6$ according to Priest 1982), m_p the proton mass and n the total particle number density. In contrast to Paper I, we also consider here disturbances at very low heights, where we cannot assume $v_\mathrm{A} \gg c_\mathrm{s}$, as is usually done in studies of type II bursts. In this case, the most important characteristic speed is the fast-mode speed, defined as

$$v_\mathrm{fm} = \sqrt{\frac{1}{2}\left\{v_\mathrm{A}^2 + c_\mathrm{s}^2 + \sqrt{\left(v_\mathrm{A}^2 + c_\mathrm{s}^2\right)^2 - 4v_\mathrm{A}^2c_\mathrm{s}^2\cos^2\theta_B}\right\}} \tag{2}$$

where θ_B is the inclination between the wave vector and the magnetic field $\boldsymbol{B}$ and c_s the sound speed. The orientation of $\boldsymbol{B}$ follows from the model, but the wave vector (i.e. the real trajectory of the disturbance) is not known a priori. Therefore, we consider here only the magnetosonic speed

$$v_\mathrm{ms} = \left(v_\mathrm{A}^2 + c_\mathrm{s}^2\right)^{1/2} \tag{3}$$

which is the fast-mode speed for $\theta_B = 90°$. For flare waves, this is reasonable, since they propagate along the solar surface where the magnetic field is predominantly radial[1]. For an arbitrary inclination towards $\boldsymbol{B}$, v_ms gives an upper limit for v_fm, while v_A is the lower limit (for $\theta_B = 0°$).

To compute the physical parameters we are interested in, we need to model the total particle number density n (this can be obtained from the electron number density via $n = 1.92\,n_\mathrm{e}$ for $\bar{\mu} = 0.6$) as well as the magnetic field $\boldsymbol{B}$. In contrast to Paper I, we include the density enhancement in the active region (AR). The derivation of a suitable density model is discussed in Sect. 3.1.

The magnetic field $\boldsymbol{B}$ is composed of the field of an active region B_AR and of the quiet Sun B_qs, i.e.

$$\boldsymbol{B} = \boldsymbol{B}_\mathrm{AR} + \boldsymbol{B}_\mathrm{qs}. \tag{4}$$

The AR is modeled by a magnetic dipole, its center located at a depth d_dip below the photosphere, while the quiet Sun magnetic field is represented by a radial field (resulting in a $1/R^2$-behavior of the field strength). The latter assumption is justified by several observations: the magnetic field in the quiet Sun is predominantly oriented radially (as shown by vectormagnetograms and EUV imaging), and to a first approximation, it does not show conspicuous variations with latitude. This independence of latitude was also observed by *Ulysses* in the radial component of the interplanetary magnetic field (IMF; see Smith & Balogh 1995; Forsyth et al. 1996).

[1] Our calculations have shown that in the low corona, the error in velocity is below 5%.

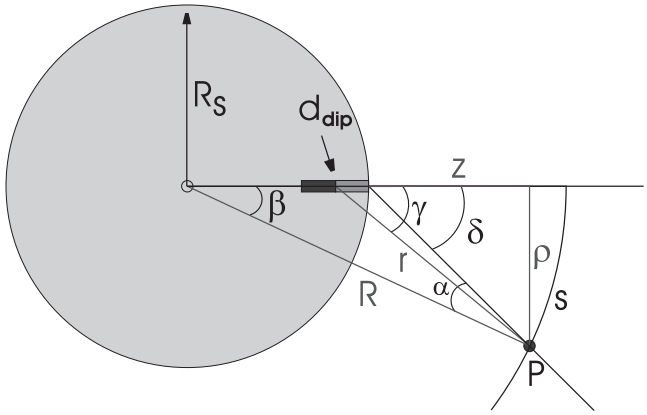

Fig. 1. Geometry of the model and frame of reference.

The geometry of the model is shown in Fig. 1. Each point P can be characterized either by the polar coordinate system with the variables R and β (with the solar center as origin of the coordinate system) or by r and γ (with the dipole center as origin). Cylindrical coordinates (z and ρ) can also be used to describe the model: in this system, the dipole is directed along the z-axis, and azimuthal symmetry is assumed around the z-axis (see also Paper I).

The magnetic field of the dipole (in cylindrical coordinates) is then given by

$$B_{\mathrm{AR},z}(r) = B_\mathrm{d0}\cdot\left(\frac{d_\mathrm{dip}}{2r}\right)^3\cdot\left(3\cos^2\gamma - 1\right) \tag{5}$$

$$B_{\mathrm{AR},\rho}(r) = B_\mathrm{d0}\cdot\left(\frac{d_\mathrm{dip}}{2r}\right)^3\cdot\left(3\cos\gamma\sin\gamma\right) \tag{6}$$

where r is the distance from the dipole center and B_d0 is the magnetic field strength on the axis of the dipole (i.e. $\gamma = \beta = 0°$) at a distance $r = d_\mathrm{dip}$ (i.e. at the photosphere, corresponding to a heliocentric distance R of one solar radius)[2].

The magnetic field of the quiet Sun is given by

$$B_{\mathrm{qs},z} = B_\mathrm{q0}\cdot\cos\beta\cdot\left(\frac{R_\mathrm{S}}{R}\right)^2 \tag{7}$$

$$B_{\mathrm{qs},\rho} = B_\mathrm{q0}\cdot\sin\beta\cdot\left(\frac{R_\mathrm{S}}{R}\right)^2. \tag{8}$$

Here, B_q0 is the magnetic field strength in the quiet Sun at $R = 1\ R_\mathrm{S}$ (where R_S is the solar radius).

Along the z-axis, the dipole can be directed either parallel or antiparallel to the quiet Sun magnetic field. Both cases model a unipolar active region. However, most ARs are actually bipolar. Therefore, an additional case which yields a bipolar configuration is considered, namely a dipole that is inclined by 90° with respect to the z-axis (this is denoted by ϕ, the angle between the dipole axis and z-axis, so that the vertical dipole corresponds to $\phi = 0°/180°$ and the horizontal dipole to $\phi = 90°/270°$). In this case, the dipole has a magnetic moment which is twice as strong as in the vertical case in order to give the same value of B_d0 as in the vertical case. Note that in the horizontal case the resulting field is no longer azimuthally symmetric around the z-axis.

[2] For details on the derivation of Eqs. (5) and (6), see Paper I.

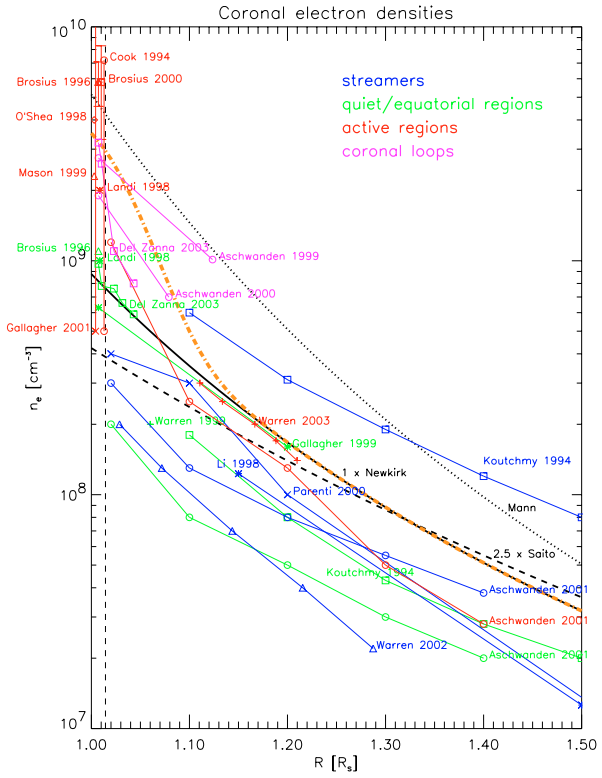

Fig. 2. Coronal electron densities, n_e, against heliocentric distance, R. The dashed verical line at $R = 1.014\ R_S$ indicates the coronal base: data points below that line have to be considered as lying at the coronal base. The thick orange dash-dotted line represents $n_e(R, \beta = 0°)$ as given by our model.

After $\boldsymbol{B}$ and n are calculated at each point P in the part of the corona that we are interested in, we can derive the required coronal parameters.

3. Observational constraints

In this section, we will try to constrain the free parameters of our model – the electron density model as well as B_{d0}, B_{q0}, and d_{dip} – by comparing the output of the model with actual observations. In order to derive a representative coronal model, we have to look at a sample of several events, or better, active region configurations. Since we are particularly interested in the propagation of coronal waves and shocks, we have chosen the flare wave events that were studied by Warmuth et al. (2004a,b) as our sample.

3.1. Density parameters

A thorough study of the literature was conducted in order to choose an appropriate coronal density model. Figure 2 depicts the coronal electron density, n_e, as a function of height R in the lower corona (up to $R = 1.5\ R_S$). It shows how some commonly used electron density models compare to actual measurements, and also gives an idea of the scatter between different measurements[3]. Included are the one-fold Newkirk model (Newkirk 1961, solid line), the 2.5-fold Saito model (Saito 1970, dashed line) and the Mann model (Mann et al. 1999b, dotted line). Table 1 lists the studies from which the measurements were taken and their primary data sources.

Table 1. Coronal electron density measurements.

Publication	Primary data source
Cook et al. (1994)	*Skylab*/SO82B
Koutchmy (1994)	WL eclipse observations
Brosius et al. (1996)	SERTS
Landi & Landini (1998)	CDS
Li et al. (1998)	UVCS, SXT
O'Shea et al. (1998)	CDS, SUMER
Aschwanden et al. (1999)	EIT
Gallagher et al. (1999)	CDS
Mason et al. (1999)	CDS
Warren (1999)	SUMER
Aschwanden et al. (2000)	EIT
Brosius et al. (2000)	SERTS
Parenti et al. (2000)	CDS, UVCS
Aschwanden & Acton (2001)	SXT
Gallagher et al. (2001)	CDS, EIT
Warren & Warshall (2002)	SUMER, SXT
Del Zanna & Mason (2003)	CDS, TRACE
Warren & Winebarger (2003)	SUMER

We have included measurements of four different coronal structures: streamers (blue lines and symbols in Fig. 2), quiet and equatorial regions (green), ARs (red) and coronal loops (magenta). In order to choose a density model for the quiet corona, we compare the various models to the measured $n_e(R)$ for streamers and quiet/equatorial regions. It is immediately evident that the Mann model, which is optimized for the heliosphere, gives density values that are too high in the inner corona. On the other hand, we find that the one-fold Newkirk model is still a good representation of the quiet coronal electron densities. As in Paper I, we therefore adopt the Newkirk model for the inner corona, which is given by

$$n_e = n_0 \times 10^{4.32 R_S/R}, \tag{9}$$

where R is the distance from the solar center, R_S the solar radius and $n_0 = 4.2 \times 10^4$ cm^{-3}). Note that the Newkirk model corresponds to a barometric height formula with a temperature of 1.4 MK. We therefore assume $T = 1.4$ MK for the whole corona, which implies an isothermal AR and a constant $c_s = 180$ km s^{-1} (obtained via $c_s = \sqrt{\gamma_{ad} k_B T/(\bar{\mu} m_p)}$, where γ_{ad} is the adiabatic exponent and k_B is the Boltzmann constant). At a height of $R = 1.8\ R_S$, we switch to the Mann model (which gives the same n_e as the Newkirk model at this height), which is more suited for the outer corona and heliosphere.

The measurements for ARs and coronal loops clearly show a density enhancement, with a scatter between different measurements that is considerably higher than for the quiet corona.

[3] For many studies we only show the density values for a few selected heights, which is sufficient to represent the behavior of n_e with respect to R. Also, the plotted values have to be considered as approximate.

Table 2. Event and active region overview. Shown are the event date, the NOAA AR number, the coordinates and importance of the associated flare, the inferred magnetic field strength of the dipole and the global component in the photosphere, B_{d0} and $B_{q,phot}$, the depth of the dipole center, d_{dip}, and the half-width of the AR, w_{AR}. The last two columns give d_{dip} and w_{AR} for the case of a horizontal dipole. Magnetic field strengths are given in Gauss, distances in Mm.

Event	NOAA	Flare	Flare			Vertical dipole		Horizontal dipole	
date	No.	loc.	imp.	B_{d0}	$B_{q,phot}$	d_{dip}	w_{AR}	d_{dip}	w_{AR}
1997 Sep. 24	8088	S31E19	1B/M5.9	2500	7	10	35	20	55
1997 Nov. 3 (a)	8100	S20W13	SB/C8.6	2800	6	15	55	20	65
1997 Nov. 3 (b)	8100	S20W15	1B/M1.4	2800	6	15	55	20	65
1997 Nov. 4	8100	S14W33	2B/X2.1	2900	7	15	55	20	65
1998 May 2	8210	S15W15	3B/X1.1	2800	7	10	50	20	65
2000 Mar. 2	8882	S20W58	SN/M6.5	2600	16	20	55	30	80
2000 Mar. 3	8882	S15W60	1B/M3.8	2600	17	20	55	30	80
2000 Nov. 25	9236	N20W23	2B/X1.9	2500	12	17	55	35	100
Mean:				2688	9.8	15	52	25	72
σ:				155	4.6	4	7	7	14

However, an electron density as given by a four-fold Newkirk model seems to be a reasonable representation of n_e at the center of an average AR.

A smooth transition from the center of the AR to the quiet corona in both the vertical and the horizontal direction is provided by means of two Gaussian profiles. By comparing with various density measurements, the *FWHM* of the Gaussian for $n_e(z)$ (vertical) was taken as $h_{AR} = 80$ Mm ($R = 1.115\,R_S$), while the *FWHM* of the Gaussian for $n_e(\beta)$ (horizontal), w_{AR}, was chosen in such a way that the density enhancement coincides with the spatial extension of the AR magnetic field. The mean values are $w_{AR} = 52$ Mm ($0.075\,R_S$) for the vertical and $w_{AR} = 72$ Mm ($0.103\,R_S$) for the horizontal dipole. The resulting $n_e(R, \beta = 0°)$ for the vertical case is shown as the thick orange dash-dotted line in Fig. 2.

3.2. Magnetic parameters

As already mentioned we use the eight events of Warmuth et al. (2004a) for which high-quality magnetograms were available to determine the most reasonable values of our "magnetic parameters" (B_{d0}, B_{q0}, and d_{dip}). These events were associated with five different active regions. The most important characteristics of the events and ARs are summarized in Table 2.

MDI full-disk magnetograms (Scherrer et al. 1995) were used to measure the unsigned magnetic flux density, B_{phot}, as a function of distance s from the center of the dominant sunspot. Figure 3 illustrates the measurement process. B_{phot} was measured within a sector (V in Fig. 3) consistent with the observed flare wave propagation, and then averaged laterally over the whole sector angle. This yields the average unsigned flux density as a function of s along the solar surface, $B_{phot}(s)$[4]. We have corrected for projection effects by dividing B_{phot} at each measured point by the cosine of the heliocentric angle.

[4] To check if the measured fluxes are consistent with the ones really experienced by the waves, we have derived $B_{phot}(s)$ also for the sector which originates at the extrapolated starting point of the flare waves (see Warmuth et al. 2004a). A comparison of the two data sets shows that the fluxes in the quiet Sun agree closely.

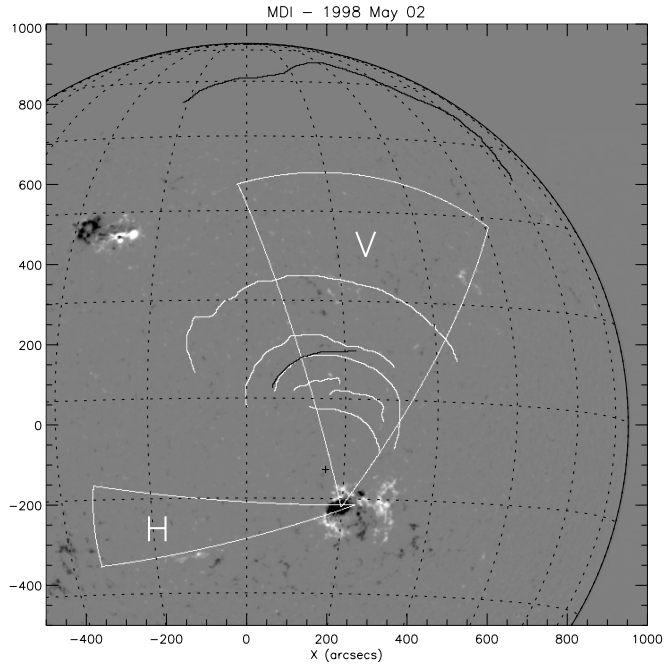

Fig. 3. Full-disk MDI magnetogram of the flare wave event of 1998 May 2. Overlayed are the Moreton (white) and EIT wavefronts (black), as well as the sectors in which B_{phot} was measured as a function of distance s. The sector used for the vertical model (V) originates in the main spot and samples the area of flare wave propagation, while the sector for the horizontal model (H) originates in the center of the AR and covers a comparatively narrow range centered on the AR axis. The black cross north of the AR denotes the extrapolated starting location of the Moreton wave. The magnetogram is linearly scaled to $B = \pm 500$ G.

By comparing the measured B_{phot} with the photospheric flux that is given by the model, it is now possible to find the most realistic values for the magnetic parameters (bearing in mind that no perfect fit is expected for such a comparatively simple model). Since the location of the origin of the measured sectors coincides with the maximum measured flux of the dominating sunspot, $B_{phot}(s = 0)$ fixes the value of B_{d0}. This location corresponds to $\beta = 0°$ in our model. d_{dip} can now be

Table 3. The quiet Sun effective coronal magnetic field strength, B_{q0}, as given by the measured photospheric magnetic flux in the quiet Sun, $B_{q,phot}$ (Col. 2), for different fractions f_{cor} of photospheric flux penetrating into the corona (Cols. 3–5). The last column shows B_{q0} as deduced from in situ measurements of the radial component of the IMF at 1 AU. All magnetic field strengths are given in Gauss.

Event date	$B_{q,phot}$	B_{q0} ($f_{cor} = 1/2$)	B_{q0} ($f_{cor} = 1/3$)	B_{q0} ($f_{cor} = 1/4$)	B_{q0} (from IP B)
1997 Sep. 24	7.0	3.5	2.3	1.8	1.4
1997 Nov. 3 (a)	6.0	3.0	2.0	1.5	1.2
1997 Nov. 3 (b)	6.0	3.0	2.0	1.5	1.2
1997 Nov. 4	7.0	3.5	2.3	1.8	1.2
1998 May 2	7.0	3.5	2.3	1.8	1.6
2000 Mar. 2	16.0	8.0	5.3	4.0	1.6
2000 Mar. 3	17.0	8.5	5.7	4.3	1.5
2000 Nov. 25	12.0	6.0	4.0	3.0	1.5
Mean:	9.8	4.9	3.3	2.4	1.4
σ:	4.6	2.3	1.5	1.2	0.2

chosen in such a way that the decrease of the modeled B_{phot} with increasing s agrees with the measured values.

To fix the parameters for the case of the horizontal dipole ($\phi = 90°/270°$), B_{phot} is measured in a different sector (H in Fig. 3). The origin is located in the center of the AR, and the measured sector samples the flux along the axis of the AR (as defined by the line between the center of the AR and the main spot). Again, the origin ($s = 0$) coincides with $\beta = 0°$ in our model.

While it is relatively straightforward to constrain B_{d0} and d_{dip}, the average unsigned magnetic flux density at the bottom of the quiet corona, B_{q0}, is very difficult to determine. In the literature, quite a broad range of numerical values is given, dependent on the observing technique and instruments used. We are aware that a precise determination of B_{q0} is beyond the scope of this work, but we nevertheless try to provide at least a best estimate.

Typical MDI magnetograms have a noise level of about 16 G (Liu & Norton, MDI website[5], SOI Tech Note SOI-TN-01-144) and are therefore not suited to derive any characteristics of weak fields. However, it is possible to average over a series of magnetograms to reduce the noise level. For seven of the eight flare wave events, high-cadence (1 min) full-disk magnetograms were available from MDI (for 1997 Sep. 24, only high-resolution magnetograms not covering the AR were available). For all events, we averaged over 30 1-min magnetograms in order to reduce the noise level from 16 G to 2.9 G. It is these averaged magnetograms that were used to measure $B_{phot}(s)$.

Recently, it has been shown that MDI gives flux densities that are on average 0.64 times lower compared to the Advanced Stokes Polarimeter (Berger & Lites 2003). By dividing our flux densities by this factor, we find the photospheric magnetic flux density in the quiet Sun, $B_{q,phot}$, to be about 10 G on average. This is in good agreement with the values recently found by Lites & Socas-Navarro (2004) through high-resolution spectropolarimetric observations. However, this value cannot simply be equated with B_{q0} at the bottom of the corona. It has been shown that the magnetic field in the quiet Sun forms a complex "magnetic carpet" (Schrijver et al. 1997), which means that a significant fraction of the magnetic flux closes down below the corona. Recently, Close et al. (2003) estimated that only 50% of the flux in a quiet region extends above 2.5 Mm (the classical height of the coronal base), while only up to ~10% extend above 25 Mm. Thus, B_{q0} is the *effective* quiet Sun magnetic field strength at the base of the corona that can be derived by $B_{q0} = f_{cor} \times B_{q,phot}$, where f_{cor} is the fraction of the magnetic flux that penetrates into the corona. While f_{cor} is certainly height-dependent, we simplify the problem by assuming a constant f_{cor} with a sharp transition at the coronal base. However, we do not really know which value of f_{cor} is appropriate. The range of B_{q0} that arises from using various values for f_{cor} is shown in Table 3.

To further constrain B_{q0}, we have to look for alternative approaches. A very promising method is to use the flare waves themselves, which was first proposed by Mann et al. (1999a). We identify the speed of the observed EIT waves (which propagate in the quiet corona) with v_{ms}. With our imposed c_s, this yields v_A and, combined with the suitable n, we finally obtain the ambient magnetic field strength. Here, we consider only the eight EIT waves of Warmuth et al. (2004a), since for these cases we are sure that they are fast-mode waves[6]. We obtain a mean EIT wave speed of $\langle v_{eit} \rangle = 310 \pm 80$ km s^{-1} (slightly higher than the speed derived by Klassen et al. 2000). Neglecting any projection effects, we assume $v_{EIT} = v_{ms}$. This is justified since the wavefronts in the different wavelength regimes – and therefore different height ranges – match up very nicely (Warmuth et al. 2004a). Thus any projection effects should be small. Now we run into the next problem – we do not exactly know the propagation height of the EIT waves, which results in an uncertainty of n. In the literature, 1.08 R_S is often found for the propagation height, but note that EIT waves observed on the limb (i.e. the events of 2000 Mar. 2 and 3, as well as the event studied by Hudson et al. 2003) are visible over a broad height range, although the excess emission is generally stronger for lower heights. For the height range

[5] http://soi.stanford.edu

[6] There are other cases of EIT waves – usually slower ones – that are more probably bulk mass motions or successive activations of field lines due to CME evolution (see e.g. Chen et al. 2002).

of $R = 1.08$–$1.005\ R_S$, the derived effective global magnetic field strengths are $B_{q0} = 2.9$–3.6 G. This nicely agrees with the magnetic field strengths derived from the magnetograms if we select $f_{cor} = 1/3$, which lies well within the range given by Close et al. (2003), and is also consistent with the results of Dere (1996).

We finally adopt $B_{q0} = 3.4$ G as the definite value for our average coronal model, which is obtained from the "wave method" with more weight towards the lower heights. Likewise, we choose $B_{d0} = 2700$ G and $d_{dip} = 15$ Mm for the vertical dipole (see Table 2). For the horizontal case, we finally adopt $d_{dip} = 25$ Mm, while B_{d0} and B_{q0} remain the same as in the vertical case (the magnetic moment, however, is twice as large). For the individual coronal models (which will be used to study flare wave propagation in Sect. 4.4), we use the parameters given in Table 2, with $f_{cor} = 1/3$.

Before continuing, we perform an independent check of B_{q0}: we compare it with the field strength given by the radial component of the IMF measured at 1 AU. We use data from the MAG magnetometer (Smith et al. 1998) aboard the *ACE* satellite, averaged over the Bartels rotation (27 days, roughly one solar rotation) during which the wave event happened. Averaged over the events, this yields a radial component of the magnetic field strength of 3 nT at 1 AU, which, when back-extrapolated using flux conservation, gives 1.4 G at the solar surface (see Table 3). This is inconsistent with our derived B_{q0}. However, the assumption of a purely radial behavior of the large-scale magnetic field is not exact, although it is quite a good approximation out of the ecliptic plane (Banaszkiewicz et al. 1998). Moreover, our radial field represents the corona which is closed on larger scales, and not the truly open regions – those would be coronal holes, with densities of at least an order of magnitude less than in our model. So apart from the transition in field strength at the coronal base (represented by f_{cor}), there is another drop in B in the height range where the larger-scale field lines close. This probably happens near the source surface at $R \approx 2.5\ R_S$. Since we are primarily interested in the corona below, say, $R < 2\ R_S$, we neglect this further complication.

Figures 4 and 5 compare the measured $B_{phot}(s)$ with the modeled values for all events (thick lines indicate the radial component of the magnetic field, thin lines the total field strength), for the vertical and the horizontal dipole, respectively. The agreement between the model and the measured $B_{phot}(s)$ is much better for the vertical scenario than for the horizontal one. In all cases, the dominating spot has a considerably larger distance from the center of the AR ($s = 0$ in Fig. 5) than can be modeled by the horizontal dipole. However, we note that the fall-off of $B_{phot}(s)$ is reproduced reasonably well also in the horizontal case, at least for larger distances. The vertical dipole, on the other hand, models the measured fields quite well also near the origin, which coincides with the center of the main sunspot. In some cases (e.g. for 1998 May 2), even the minimum of B in the range of $s = 50$–100 Mm can be discerned in the measured $B_{phot}(s)$.

Thus, we are confident that the parameters we derived for the vertical case are sufficiently realistic to form the basis of a representative, yet simple, coronal model. This "vertical model" may not reflect the bipolar nature of an AR, but it is useful to study ARs with a single dominant sunspot – most of the ARs discussed here show such a tendency. In our study of flare wave propagation, we will therefore use only the vertical model.

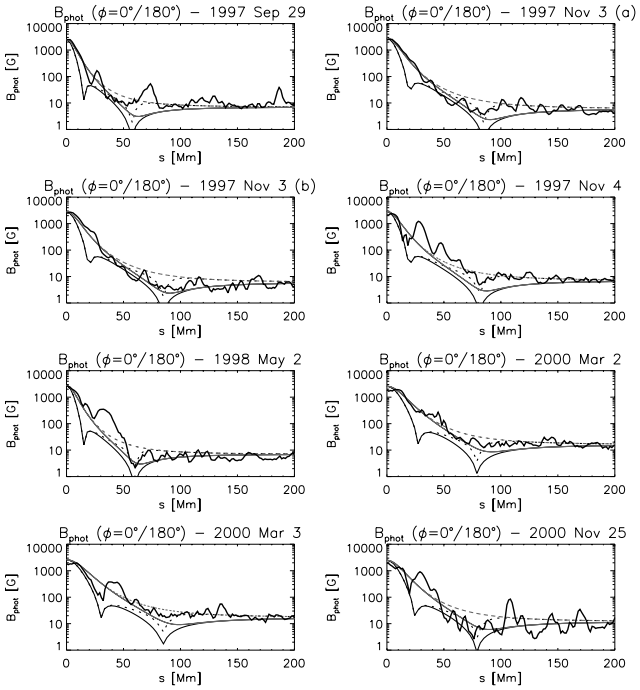

Fig. 4. Comparison of the modeled photospheric unsigned magnetic flux density $B_{phot}(s)$ with the measured values (thick grey line) taken from MDI magnetograms. The radial component of the modeled magnetic field is shown as a thick black line (solid for $\phi = 0°$, dashed for $\phi = 180°$), while the total field strength is denoted by the thin grey lines.

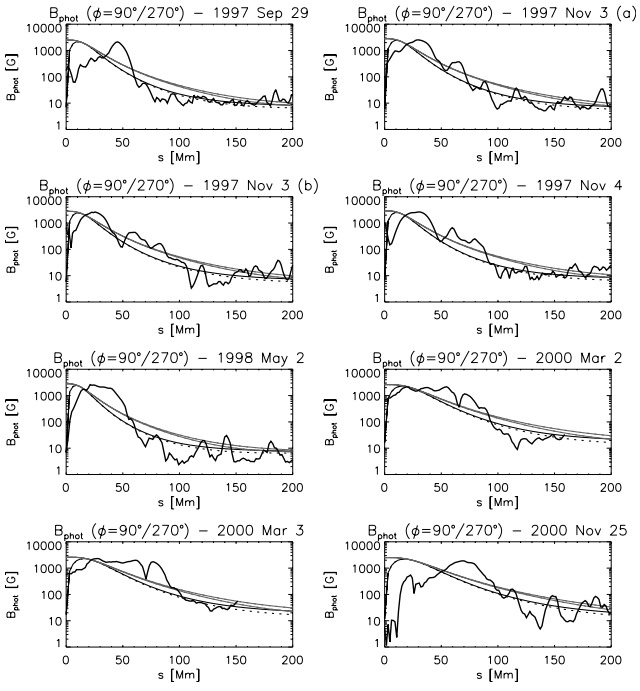

Fig. 5. As in Fig. 4, but for the horizontal dipole ($\phi = 90°/270°$).

4. Discussion

4.1. Numerical values of free parameters

Our derived magnetic parameters are different from the ones used in Paper I. There, $B_{d0} = 800$ G, $B_{q0} = 2.2$ G, and $\lambda/2 = d_{dip} = 35$ Mm ($0.05\,R_S$)were used, which were taken from the literature. However, we are confident that the parameters derived in the present work, which are based on actual measurements, provide a more realistic picture of the corona.

It came as a surprise that we obtained values for d_{dip} that were on average between 1.4 (horizontal dipole) and 2.3 times (vertical dipole) smaller than in Paper I. The original reason to select $d_{dip} = 35$ Mm was to locate the center of the dipole in the middle of the convection zone. However, recent results from helioseismological studies with MDI suggest that sunspots and active regions may be comparatively "shallow" phenomena. For example, Zhao et al. (2001) have reported a depth of 5–6 Mm for a sunspot (as defined by its thermal and hydrodynamic properties), while they find strong mass flows across the spot at depths of 9–12 Mm. While no quantitative agreement between our simple model and the helioseismological results is to be expected, these recent observations nevertheless show that it is not unreasonable to locate the origin of sunspots and ARs closer to the solar surface than it has formerly been assumed.

4.2. Solar cycle dependencies of model parameters

The events/active regions that were used to derive our model parameters were observed both during the ascending phase of solar cycle 23 (1997 and 1998), and near its maximum (2000). This enables us to study cycle dependencies of these free parameters. Table 2 reveals that B_{d0} shows no such variation, while both $B_{q,phot}$ and d_{dip} are larger near solar maximum. The variation of $B_{q,phot}$ is consistent with the well-known fact that the solar weak-field component increases by a factor of ≈2 from minimum to maximum (e.g. Rabin et al. 1991; Pevtsov & Acton 2001). This increase is mainly due to the increasing area of the comparatively strong network fields (cf. Pauluhn & Solanki 2003). No explanation for the variation of d_{dip} is known – of course, poor statistics cannot be ruled out.

4.3. Distribution and numerical values of characteristic coronal parameters

Figure 6 shows v_{ms} as derived from our model (we do not show v_A since it can always be obtained from v_{ms} via Eq. (3)). The arrows indicate the direction of the magnetic field. The corona is shown from its base up to $R = 2\,R_S$, within a sector of $\beta = \pm 45°$. From left to right, the cases for the parallel, antiparallel and horizontal dipole are shown ($\phi = 0°/180°/90°$, the configuration for $\phi = 270°$ is obtained by simply mirroring the $\phi = 0°$ model at the z-axis). Note that the model parameters that were used for the horizontal case are different from those for $\phi = 0°/180°$ (cf. Sect. 3). The horizontal case is not azimuthally symmetric, and in order to give an idea of the 3D configuration, Fig. 7 shows v_{ms} in the yz-plane, orthogonal to the xz-plane depicted in Fig. 6.

It is immediately evident that the AR influences the coronal structure quite dramatically. In the parallel case, local minima of v_{ms} are found low in the corona, at a distance of $s \approx 120$ Mm from the AR center, with an absolute minimum of $v_{ms} = 220$ km s^{-1}. In the antiparallel case, on the other hand, a pronounced minimum (with a minimum value of $v_{ms} = 180$ km s^{-1}; this also means $B = 0$) sits above the AR at a height of ≈150 Mm ($R = 1.2\,R_S$). This behavior was implicitly found in Paper I, but the 2D representation gives a much clearer image of the coronal structure. We note that a minimum above the AR is also present in the parallel case, but there it is much less pronounced. The same is true for the minima flanking the AR in the antiparallel case. In the center of the ARs, on the other hand, we find v_{ms} of the order of several 10 000 km s^{-1}. For large distances s, we find $v_{ms} = 300$ km s^{-1} at the coronal base.

The horizontal case shows a different morphology: in the xz-plane, a local minimum of v_{ms} (at a height of ≈240 Mm; as in the antiparallel case, the lowest value is $v_{ms} = 180$ km s^{-1}) is found in one hemisphere, while the other hemisphere is characterized by a finger-like enhancement of v_{ms}. In the yz-plane, the distribution of v_{ms} is morphologically similar to the parallel case. Generally, in the horizontal case the coronal structures are more extended as compared to the vertical one, which is a consequence of the larger value for d_{dip} that was used for the horizontal dipole.

Further out in the upper corona, a broad maximum of v_{ms} is found, in accordance with the results of Paper I. It peaks with $v_{ms} = 1100$ km s^{-1} at a height of $R = 3.5\,R_S$. This maximum is basically similar for all three model configurations. In Paper I, the maximum was less pronounced and located slightly higher, with $v_{ms} = 740$ km s^{-1} and $R = 3.8\,R_S$. Note that the maximum will become less pronounced if the large-scale field lines are closing below $R \approx 3.5\,R_S$ (cf. Sect. 3.2).

In order to study how the coronal structures change when we use different model parameters, a series of different models was computed by varying B_{d0}, B_{q0} and d_{dip}. We found that an increase in B_{d0} leads to a growth of the extension of the coronal minima, as well as to an increase in altitude/distance from the AR. When B_{q0} is increased, the coronal minima migrate downward/inward (with respect to the AR) and become less extended. The most sensitive parameter, however, appears to be d_{dip}: when the dipole depth is increased, all coronal structures show dramatic expansion. Both the coronal minima and the AR enhancement expand in size, and the minima move farther out. On the other hand, the influence of changes in B_{d0} and d_{dip} on the location of the global coronal maximum (at $R \approx 3.5\,R_S$) are small, since the influence of the dipole decreases proportional to $1/r^3$.

Figure 8 shows the distribution of another important coronal parameter, the plasma beta β_p, which is obtained via

$$\beta_p = \frac{8\pi n k_B T}{B^2} = \frac{6c_s^2}{5v_A^2}, \tag{10}$$

where an adiabatic exponent of $\gamma_{ad} = 5/3$ has been assumed. β_p gives the ratio of the gas pressure to the magnetic one, and

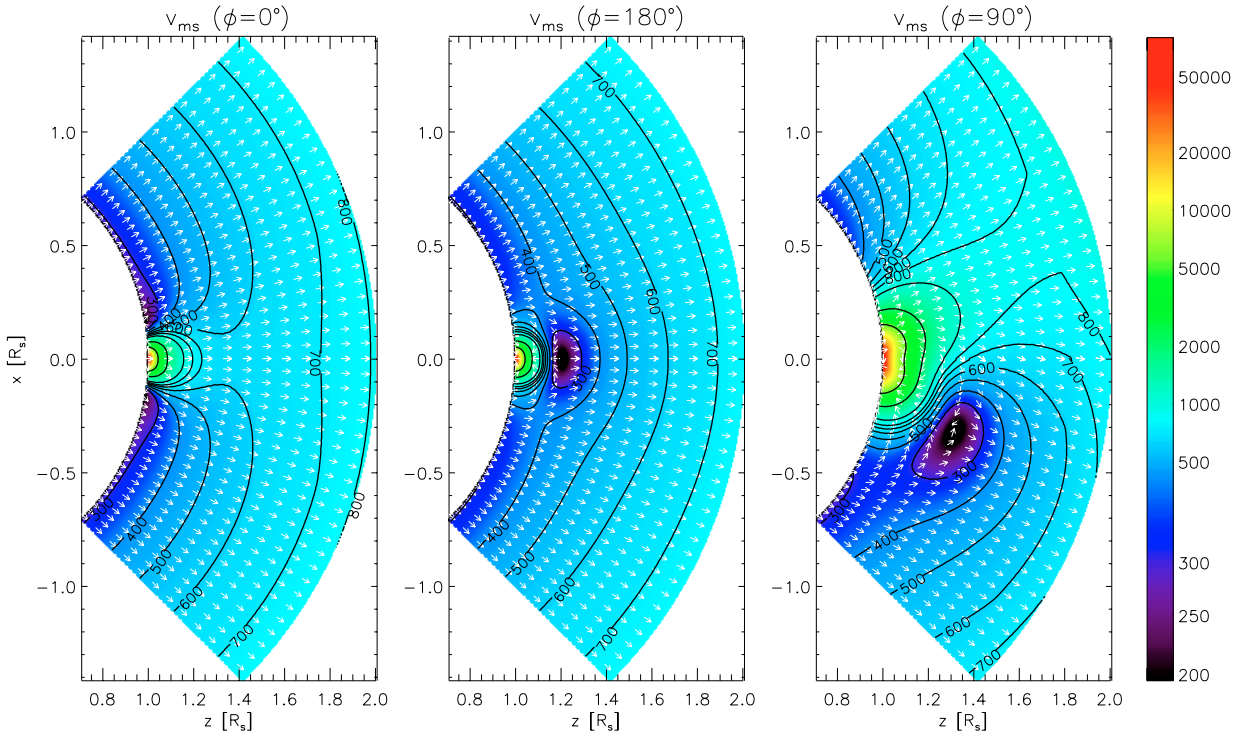

Fig. 6. Coronal distribution of the magnetosonic velocity $v_{\rm ms}$ for the cases of a parallel ($\phi = 0°$), antiparallel ($\phi = 180°$), and horizontal ($\phi = 90°$) dipole. The arrows indicate the direction of the magnetic field $\boldsymbol{B}$. $v_{\rm ms}$ is given in km s^{-1}.

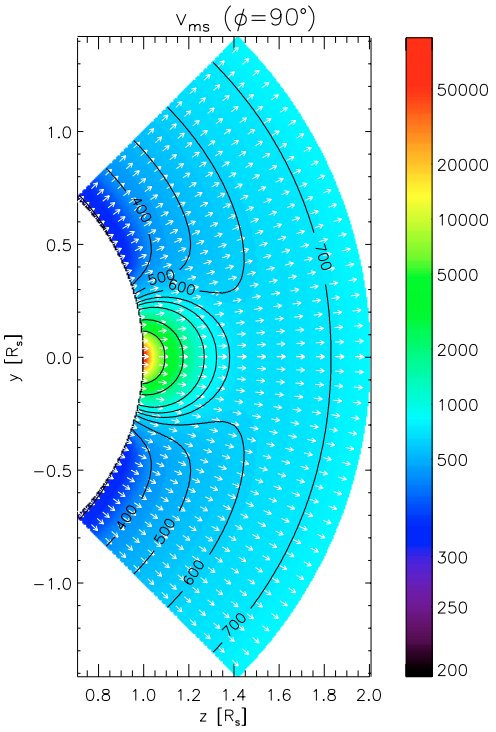

Fig. 7. Coronal distribution of $v_{\rm ms}$ in the yz-plane for the case of a horizontal dipole. $v_{\rm ms}$ is given in km s^{-1}.

usually $\beta_{\rm p} \ll 1$ is assumed in the corona. Figure 8 shows that this condition is fulfilled near the AR and in the greater part of the corona, while in the lower corona $\beta_{\rm p}$ is higher, but still less than unity (e.g. $\beta_{\rm p} = 0.65$ at the coronal base in the quiet Sun).

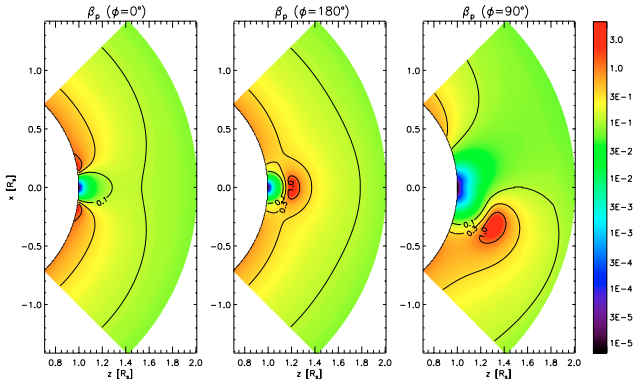

Fig. 8. Coronal distribution of the plasma beta, $\beta_{\rm p}$.

However, at the locations of the minima of $v_{\rm ms}$, $\beta_{\rm p}$ can actually become larger than 1. This is in agreement with the results of Gary (2001), who found that $\beta_{\rm p}$ can reach unity at heights as low as $R \approx 1.2\,R_{\rm S}$, which is just the height of maximum of $\beta_{\rm p}$ in our antiparallel model. While Gary's model was only 1D, we can now show the actual locations of these maxima within the context of the AR. Interestingly, they are consistent with the location of the cusp of helmet streamers, where $\beta_{\rm p} > 1$ is required. Note that depending on the inclination of the dipole, our simple model can reproduce the $\beta_{\rm p}$-enhancement required for both radial (antiparallel case) and nonradial streamers (horizontal case)[7].

Very recently, the first reliable direct measurements of coronal magnetic field strengths have become available through

[7] Naturally, our model cannot account for a streamer itself.

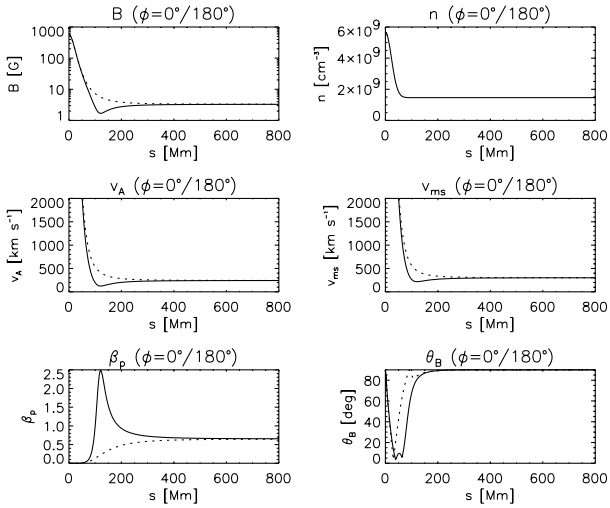

Fig. 9. Coronal parameters $B, N, \beta_\mathrm{p}, v_\mathrm{A}, v_\mathrm{ms}$, and θ_B, plotted as function of distance s from the center of the AR, for a height of $h = 10$ Mm. Solid and dashed lines are for $\phi = 0°/180°$, respectively.

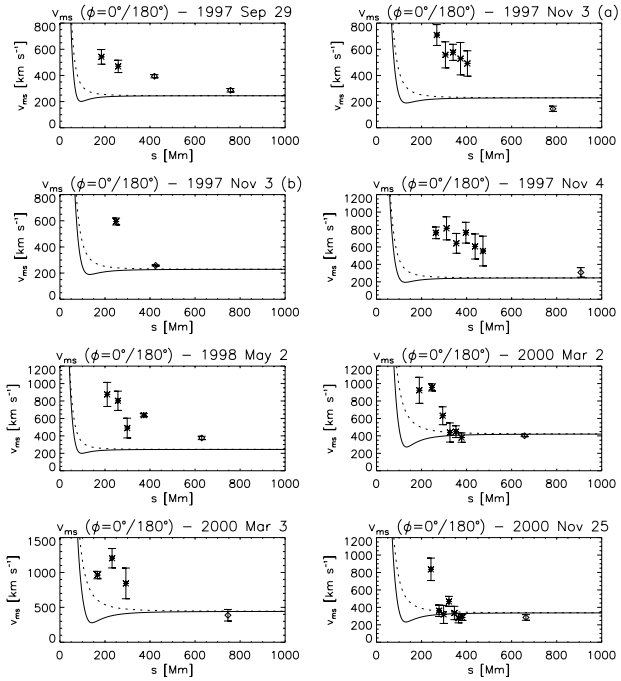

Fig. 10. Comparison of the modeled magnetosonic speed $v_\mathrm{ms}(s)$ (computed along a circular trajectory following the curvature of the solar surface at a height of 10 Mm) with measured flare wave speeds for all studied events. The solid and dashed lines are the v_ms derived for the parallel and antiparallel dipole ($\phi = 0°/180°$), respectively. Asterisks denote Hα Moreton wave speeds, diamonds represent EIT wave speeds.

Zeeman splitting observations of infrared coronal emission lines (Lin et al. 2004). At heights of $R = 1.1$–$1.4\ R_\mathrm{S}$, field strengths of 4–2 G have been found, which is generally in agreement with the values given by our model.

4.4. Propagation of flare waves

For the study of flare waves, it is instructive to trace the coronal parameters at a fixed height (which should be close to the probable propagation height of the disturbance), following a curved trajectory parallel to the solar surface. In Fig. 9, we have plotted B, N, β_p, v_A, v_ms, and the inclination of the magnetic field to the curved trajectory, θ_B, as function of distance s from the center of the AR, for a height of $h = 10$ Mm. This height should reflect the typical conditions near the coronal base, where the disturbance that subsequently generates the chromospheric Moreton signatures propagates. In addition, it is high enough so that no density enhancement is to be expected from a possibly extended chromosphere (cf. the spicular extended chromosphere model inferred from radio limb measurements; see Ewell et al. 1993; for a recent confirmation of this scenario by means of *RHESSI* hard X-ray observations, see Aschwanden et al. 2002).

As pointed out in Sect. 3.2, we are only considering the vertical dipole model. The fall-off of the characteristic speeds with increasing distance s from the AR is clearly seen (with a distinct minimum for $\phi = 0°$). Conversely, β_p rises from $\beta_\mathrm{p} \ll 1$ to $\beta_\mathrm{p} = 0.65$, with a local maximum of $\beta_\mathrm{p} = 2.5$ for $\phi = 0°$. The behavior of θ_B is somewhat more complicated: it declines rapidly from 90° (which means radial orientation of $\boldsymbol{B}$) to a minimum of $\theta_B < 10°$, but then returns quickly to $\theta_B = 90°$. In contrast to v_ms and β_p, the minimum of θ_B exists in both the parallel and antiparallel cases. Also note that while the minimum of v_ms and the maximum of β_p are both located at $s \approx 120$ Mm, the minimum of θ_B is considerably closer at $s = 30$–70 Mm. The mean distance between the center of the main spot of the AR (i.e. the dipole center at $s = 0$) and the extrapolated starting location of the Moreton waves inferred by Warmuth et al. (2004a) is 88 ± 28 Mm. This implies that the assumption of $v_\mathrm{ms} = v_\mathrm{fm}$ is valid over the flare wave propagation distance, since the only significant deviation from $\theta_B \approx 90°$ is closer to the AR center and can thus be neglected for our purposes.

We will now compare the measured Moreton and EIT wave speeds of our eight events with the modeled v_ms. In order to make a sensible comparison, we are not using our average model, but the individual models for the various events, using the model parameters of Table 2. In Fig. 10, we have plotted $v_\mathrm{ms}(s)$ for all events, computed for a propagation height of $h = 10$ Mm (i.e. at the coronal base). Asterisks denote the speeds derived from consecutive Moreton wavefront pairs (in the event of 1997 Nov. 3 (b), the speed of an X-ray wave is depicted instead), while diamonds represent EIT wave speeds. It is evident that the waves are decelerating – the Moreton wave speeds are declining with s and are always higher than the EIT wave speeds. This was already pointed out by Warmuth et al. (2001) and Vršnak et al. (2002a). It is also evident that the Moreton speeds are usually considerably higher than v_ms. The speeds at small distances are always well above than v_ms, and only in two events they eventually decline to levels comparable with v_ms.

The EIT wave speeds, on the other hand, are always comparable to v_ms. This is of course no surprise, since we have assumed in our determination of the magnetosonic speed that $v_\mathrm{ms} = v_\mathrm{EIT}$. If we accept that this is true, then Fig. 10 shows that

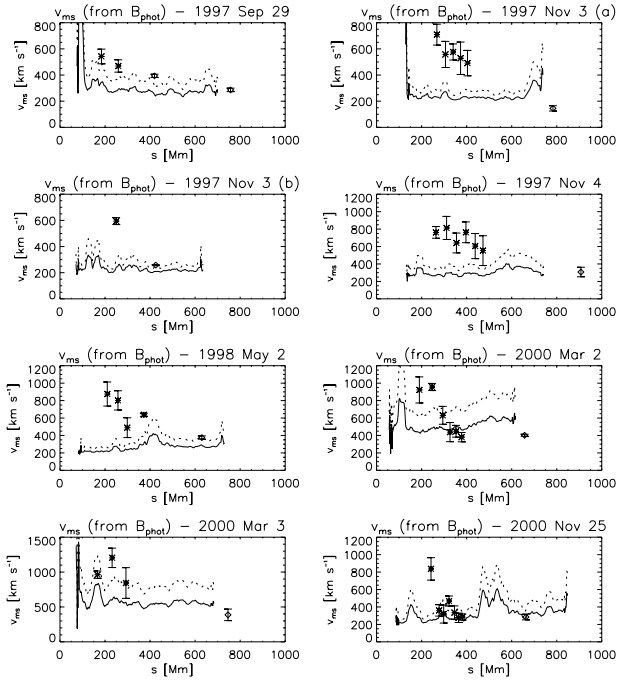

Fig. 11. Comparison of the magnetosonic speed $v_{\rm ms}(s)$ derived from the measured $B_{\rm phot}(s)$ with measured flare wave speeds for all studied events. The solid and dotted lines are the $v_{\rm ms}$ derived for $f_{\rm cor} = 1/3$ and 1/2, respectively. Asterisks denote Hα Moreton wave speeds, diamonds represent EIT wave speeds.

all of the studied waves are initially clearly supermagnetosonic. For the Moreton wave speeds derived from the earliest wavefront pairs, the mean magnetosonic Mach number (defined as $M_{\rm ms} = v_{\rm wave}/v_{\rm ms}$) is $\langle M_{\rm ms}\rangle = 3.0 \pm 0.4$ for the parallel dipole, and $\langle M_{\rm ms}\rangle = 2.5 \pm 0.6$ for the antiparallel case.

In order to cross-check our results, we have also compared the wave speeds with $v_{\rm ms}$ derived from the measured $B_{\rm phot}(s)$, which is shown in Fig. 11. Note that the sectors used for measuring $B_{\rm phot}(s)$ differ from the ones used for deriving the magnetic parameters in Sect. 3.2 in the sense that they are originating at the extrapolated wave starting location instead of the main spot's center. They thus coincide with the sectors in which the waves were measured by Warmuth et al. (2004a). The solid lines in Fig. 11 represent $v_{\rm ms}$ computed for $f = 1/3$. The derived $v_{\rm ms}(s)$ is considerably more irregular than the modeled one, but still we find that at least the first Moreton velocities are considerably higher than $v_{\rm ms}$, while the EIT wave speeds are comparable to $v_{\rm ms}$. The mean magnetosonic Mach number for the first wave speeds is $\langle M_{\rm ms}\rangle = 2.6 \pm 0.9$, comparable to the modeled ones.

Our findings imply that the waves are, at least initially, strongly supermagnetosonic. Usually, flare waves are considered as weak fast-mode shocks (e.g. Narukage et al. 2002), but at least for our event sample this is not the case. Warmuth et al. (2004b) have proposed that pronounced Hα signatures require particularly strong disturbances, which presumably will be faster.

Still, it might be argued that the initial Mach numbers are too high. The wave speed measurements are accurate, therefore a higher $v_{\rm ms}$ would be required to obtain a lower $M_{\rm ms}$. This could be achieved either with a decrease in density n, a higher $B_{\rm q,phot}$, or a larger $f_{\rm cor}$. Decreasing n by a factor of 2 would increase $v_{\rm ms}$ in the quiet corona only by a factor of 1.3, and a further decrease of n would be inconsistent with the observations. A higher $B_{\rm q,phot}$, on the other hand, would imply that magnetographic observations are still missing a considerable percentage of magnetic flux. Recent observations by Lites & Socas-Navarro (2004) suggest that this is not the case. $f_{\rm cor}$ is the parameter that is least well known – it is possible that it is larger than we have assumed, but probably not larger than 1/2 (Dere 1996; Close et al. 2003). To illustrate this possibility, the dotted lines in Fig. 11 show $v_{\rm ms}$ for $f_{\rm cor} = 1/2$. It is evident that the waves are initially still highly supermagnetosonic – using $f_{\rm cor} = 1/2$, the mean magnetosonic Mach numbers are $\langle M_{\rm ms}\rangle = 2.2 \pm 0.4$ for the parallel and $\langle M_{\rm ms}\rangle = 2.0 \pm 0.6$ for the antiparallel dipole model, and $\langle M_{\rm ms}\rangle = 2.0 \pm 0.8$ for $v_{\rm ms}$ derived from $B_{\rm phot}(s)$.

Certainly even lower Mach numbers could be achieved using a combination of the three possibilities mentioned above, but not without introducing a major inconsistency: the EIT wave speeds would be significantly lower than $v_{\rm ms}$. This would be possible if EIT waves were not really waves at all, but rather bulk mass motions or successive activation of magnetic field lines in the framework of a CME eruption (e.g. Chen et al. 2002). While there may indeed exist such EIT "waves" (EIT waves have a quite diverse morphology), we are confident that the EIT signatures in our events have been created by the same fast-mode wave as the associated Moreton fronts. A second possibility to explain $v_{\rm EIT} < v_{\rm ms}$ would be to invoke strong damping caused by a high viscosity. Ballai & Erdélyi (2004), for example, have used the velocity attenuation of EIT waves to derive viscosity coefficients over an order of magnitude higher than the classical value. However, many EIT waves show no significant deceleration over long distances (B. J. Thompson, private communication). Moreover, in two of our events (2000 Mar. 2 and 2000 Nov. 25, see Fig. 10) the last measured Moreton wave velocities are comparable to the EIT velocities, which were measured at much greater distances. This is at odds with the notion of strong damping, which predicts that the velocities at larger distances should be significantly lower. Other support for $v_{\rm EIT} = v_{\rm ms}$ comes from numerical simulations (e.g. Wang 2000; Wu et al. 2001).

In conclusion, we find that the arguments for a much larger $v_{\rm ms}$ are not convincing. The most natural explanation for the kinematical behavior is that flare waves are signatures of a shock or a large-amplitude simple wave (Mann 1995; Vršnak & Lulić 2000). As this disturbance propagates, its amplitude decreases due to the fact that the leading edge moves faster than the trailing one, as well as due to geometric expansion and dissipative processes, which results in deceleration. Finally $M_{\rm ms} = 1$ will be reached – the shock/large-amplitude wave has decayed to an ordinary fast-mode wave. This scenario is also supported by the evolution of the perturbation profiles of the waves (Warmuth et al. 2004a), which show a steady increase in perturbation thickness and a decrease in amplitude with increasing distance s.

4.5. Propagation of type II radio bursts

All flare wave events we have studied in the present work were also associated with type II bursts. We will therefore study how these signatures of coronal shocks fit into the scenario we have developed above. A detailed comparison of the type II kinematics with our model in the sense as it was done for the flare waves is not possible, since we know only the velocity component against the density gradient (derived from the observed frequency drift rate)[8]. We thus use only the integral parameters of the bursts as determined by Warmuth et al. (2004b). We have recalculated the velocities using a onefold Newkirk model, since this is consistent with our coronal model at the type II propagation heights.

Averaged over the four type II bursts in our event sample that could be reliably measured, we obtain an initial speed of $\langle v_0 \rangle = 1230 \pm 250$ km s^{-1} and a mean propagation speed of $\langle \bar{v} \rangle = 880 \pm 230$ km s^{-1}. Considering these two speeds (taken as constant) as representative for the burst propagation, we compute profiles of $M_{\rm ms}$ along straight trajectories originating in the AR center for various inclinations δ (see Fig. 1), since type II bursts can have distinctly non-radial trajectories (e.g. Klassen et al. 1999). v_0 and $\bar{v}$, on the other hand, are basically radial velocities. We divide them by the cosine of α (with $\alpha = \delta - \beta$, see Fig. 1) to get the true speed.

One important caveat is that in reality the emission-producing region of the shock will not follow a straight trajectory. Firstly, the coronal wavefront will refract towards regions of low $v_{\rm A}$ (cf. Uchida et al. 1973). This effect will be stronger for larger angles δ, and since we restrict ourselves to $\delta < 45°$, we estimate that the effect will not be so large as to render our approach invalid. In addition, strong tilting away from the radial direction will only happen very close to the solar surface, whereas at greater heights the gradient of $v_{\rm A}$ is becoming increasingly radial.

Secondly, the angle between the magnetic field vector and the wave/shock normal, θ_B, plays an important role in particle acceleration, and thus radio wave generation. For example, efficient electron acceleration through shock drift acceleration requires $\theta_B > 80°$ under coronal conditions (Mann 1997). Calculating θ_B along different straight trajectories, we have found that this condition is fulfilled only over very short distances (<0.1 $R_{\rm S}$). Of course, the disturbance producing the type II emission does not propagate in a single direction, but has a significant angular width. Type II emission would then be generated only at the locations where $\theta_B > 80°$, and the burst source would move also *along* the shock surface in addition to the overall outward expansion, or it may even jump rapidly between different locations along the front of the perturbation. The true complexity of the distribution of θ_B – even in the case of a simple dipole – is shown in Fig. 12. Since the exact trajectories and width of the type II-producing disturbance are not known, θ_B is shown with respect to the surface normal.

An extended shock will always encounter regions of $\theta_B > 80°$, providing for continuous type II emission. In that case, the drift rate would not necessarily yield true kinematical information about the physical disturbance, since different regions of the corona are sampled in quick succession. However, the simple fact that most type II bursts appear to be not too irregular puts a constraint on this scenario. An alternative possibility is to invoke shock diffusive acceleration at quasi-parallel shocks ($\theta_B < 10°$; see e.g. Mann & Lühr 1994; Mann & Classen 1995), which is more easily achieved with a simple radial propagation of the burst-generating shock. In any case, we believe that the range given by $\langle \bar{v} \rangle$ and $\langle v_0 \rangle$ is a reasonable approximation of the true speed of a coronal shock, since the associated Moreton waves initially have about the same velocities (see Warmuth et al. 2004b).

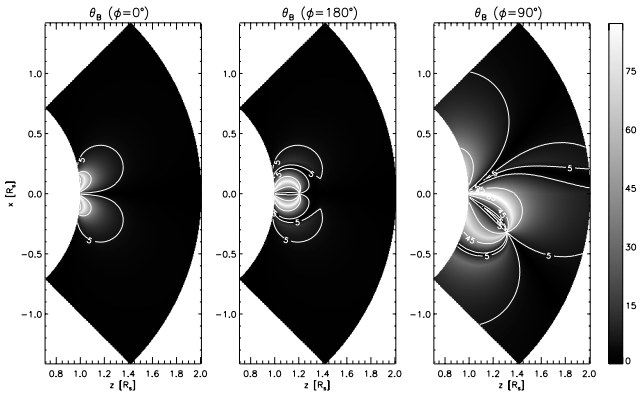

Fig. 12. Coronal distribution of the inclination between the solar surface normal and the magnetic field, θ_B.

Bearing in mind these limitations, the calculated profiles of $M_{\rm ms}$ – shown in Figs. 13 and 14 – should be regarded as giving a first idea of the behavior of $M_{\rm ms}$ in an expanding coronal shock. In the case of the vertical dipole, $M_{\rm ms}$ becomes larger than unity at heights of $R \approx 1.1$–$1.2\ R_{\rm S}$ (note that $M_{\rm ms}$ has to be well above unity in order to excite radio emission). $M_{\rm ms}$ rises to a maximum (due to the local minimum of $v_{\rm ms}$) and then declines again. For the parallel dipole, this maximum is broad and comparatively shallow, with $M_{\rm ms} \approx 1.5$–3 at $R \approx 1.2$–$1.4\ R_{\rm S}$. In the antiparallel case, the maximum is much more pronounced with $M_{\rm ms} \approx 3$–8 at $R \approx 1.2$–$1.4\ R_{\rm S}$. The same basic behavior is found for the horizontal model, with the difference that the maximum of $M_{\rm ms}$ becomes more pronounced for increasing δ.

Accordingly, the type II bursts will become visible at heights of $R \approx 1.1$–$1.2\ R_{\rm S}$ ($R \approx 1.2$–$1.4\ R_{\rm S}$ for the horizontal model). In all cases $M_{\rm ms}$ approaches or drops below unity at $R \approx 2$–$3\ R_{\rm S}$, which is due to the global maximum in $v_{\rm ms}$. This is consistent with the observation that most metric type II bursts do not continue into the outer corona.

The mean starting frequency for the four well-defined type II bursts in our sample is $f_0 = 148$ MHz, while it is $f_0 = 123$ MHz if also the questionable measurements are taken into account. By comparing f_0 to our electron density model, we find that the type II bursts first become visible at heights of $R = 1.14$–$1.18\ R_{\rm S}$, respectively. This is exactly within the expected range of $R = 1.1$–$1.2\ R_{\rm S}$ given by the model. As the initial disturbance encounters the local minimum of $v_{\rm ms}$, it will steepen rapidly to a large-amplitude wave or shock. Both kinds

[8] Co-temporal radioheliographic observations would allow for a better characterization of the kinematics, but are unfortunately available only for a limited event sample.

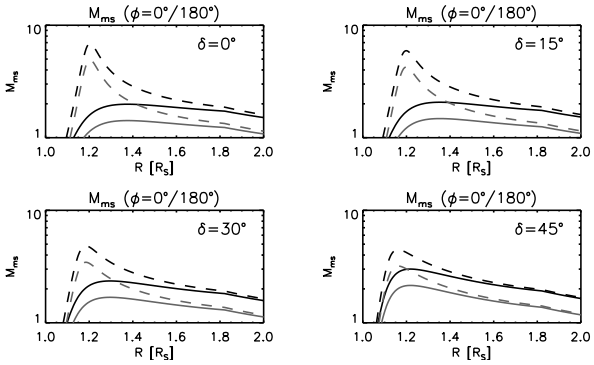

Fig. 13. Magnetosonic Mach number $M_{\rm ms}$ along straight lines with various inclination δ towards the z-axis, as calculated with the vertical dipole model. Black lines are for $v_0 = 1230$ km s^{-1}, grey lines for $\bar{v} = 880$ km s^{-1}. Solid and dashed lines are for $\phi = 0°$ and $\phi = 180°$, respectively.

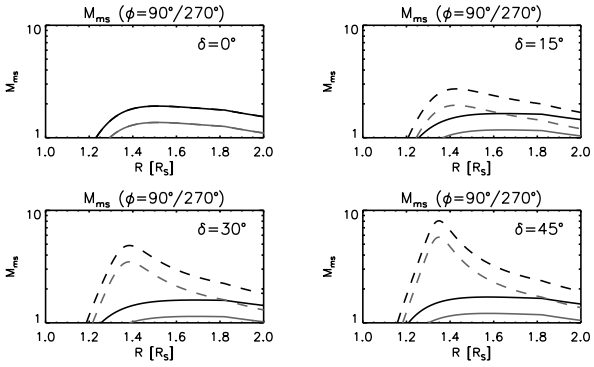

Fig. 14. As Fig. 13, but for the horizontal dipole model. Solid and dashed lines are for $\phi = 90°$ and $\phi = 270°$, respectively.

of perturbations are able to accelerate electrons, thus producing type II radiation.

The relative band-split (see Smerd et al. 1974; Vršnak et al. 2002b) of the type II bursts was used by Warmuth et al. (2004b) to deduce mean magnetosonic Mach numbers of $\langle M_{\rm ms} \rangle = 1.9$–$2.2$. This generally agrees with the computed values of $M_{\rm ms}$, as well as with the Mach numbers derived for the early phase of the Moreton waves. For $\phi = 180°/270°$, however, the computed maxima of $M_{\rm ms}$ are much higher than the observed ones (see Figs. 13 and 14). A possible explanation could be that the ARs in our events can best be described by a parallel dipole, where the maxima of $M_{\rm ms}$ are less pronounced than for both the antiparallel and the horizontal cases (we have already argued against the horizontal model in Sect. 4.4).

5. Conclusion

We have presented a simple model of the Alfvén speed $v_{\rm A}$ and the fast magnetosonic speed $v_{\rm ms}$ (along with other important physical parameters) in the solar corona, using the model of Mann et al. (2003) as a basis. We have improved the model by constraining the free parameters with actual observations (including the use of coronal seismology) and by considering the case of a horizontal dipole (modeling a bipolar AR). The model provides a global maximum of $v_{\rm ms} = 1100$ km s^{-1} at a distance of $R = 3.5\ R_{\rm S}$ from the center of the Sun, and several local minima at $R = 1.2$–$1.4\ R_{\rm S}$ (depending on the orientation of the dipole). At the coronal base in the quiet Sun, we obtain $v_{\rm ms} = 300$ km s^{-1}. The plasma beta $\beta_{\rm p}$, while less than unity in most of the inner corona, can approach and surpass 1 in the minima of $v_{\rm ms}$.

The fact that the model incorporates both the quiet corona and an AR allows us to study the transition between those two regimes, which are traditionally treated in isolation. This is essential for the study of the development and evolution of coronal disturbances. We have considered flare waves (Moreton and EIT wave signatures) and type II radio bursts as signatures of coronal waves and/or shocks. The events were taken from Warmuth et al. (2004a). For flare waves, we have found that the disturbances are initially highly supermagnetosonic ($M_{\rm ms} \approx 2$–3), but when they have reached typical EIT wave distances ($s > 400$ Mm), they have decelerated to $M_{\rm ms} = 1$. The most natural explanation for this behavior is that the signatures are caused by initially strong shocks or large-amplitude simple waves which decay to ordinary fast-mode waves, thus confirming the initial hypothesis of Warmuth et al. (2001).

For the associated type II bursts, we found that the measured starting heights are consistent with the region where the magnetosonic Mach number $M_{\rm ms}$ well exceeds unity, thus enabling type II emission. The measured $M_{\rm ms}$ of the bursts (using their relative band-split) is broadly consistent with the predicted values, as well as with the $M_{\rm ms}$ deduced for the flare waves. This once again shows that flare waves and type II bursts are created by the same physical disturbance.

We are aware that our model gives a very idealized picture of the solar corona, since complex ARs are not well represented by a dipole. However, this model allows us to learn about issues that will also be important in more complex configurations. For example, we can see how the local minima of $v_{\rm ms}$ vary with changes of the dipole orientation, strength, and depth, etc. As another example, consider the distribution of θ_B shown in Fig. 12: how much more complicated will the situation be in a real AR if already a simple dipole gives such rich structure?

In spite of being idealized, our model has been remarkably consistent with both the imaging and radiospectral observations of coronal disturbances. We conclude that at least the vertical dipole model is an adequate representation of the corona in the presence of an AR with a strong dominating sunspot (this was the case in all studied events). A particularly interesting finding has been the initially high magnetosonic Mach numbers in the studied flare wave events. The corresponding high compression factors suggest that particles could be accelerated to comparatively high energies. Flare waves may thus be an additional source of solar energetic particles (see e.g. Krucker et al. 1999; Vainio & Khan 2004). We plan to use our model, combined with both imaging and radiospectral data, to further explore particle acceleration at shocks or simple waves in the low corona.

Acknowledgements. The work of A.W. was supported by DLR under grant No. 50 QL 0001. We thank the ACE MAG instrument team and the ACE Science Center for providing the ACE data.

References

Aschwanden, M. J., & Acton, L. W. 2001, ApJ, 550, 475
Aschwanden, M. J., Newmark, J. S., Delaboudinière, J.-P., et al. 1999, ApJ, 515, 842
Aschwanden, M. J., Alexander, D., Hurlburt, N., et al. 2000, ApJ, 531, 1129
Aschwanden, M. J., Brown, J. C., & Kontar, E. P. 2002, Sol. Phys., 210, 383
Aurass, H. 1996, in Coronal Physics from Radio and Space Observations, ed. G. Trottet, Lecture Notes in Physics (Heidelberg: Springer Verlag), 135
Ballai, I., & Erdélyi, R. 2004, in Proc. 13th SOHO Workshop, ed. H. Lacoste, ESA SP-547, 433
Banaszkiewicz, M., Axford, W. I., & McKenzie, J. F. 1998, A&A, 337, 940
Berger, T. E., & Lites, B. W. 2003, Sol. Phys., 213, 213
Brosius, J. W., Davila, J. M., Thomas, R. J., & Monsignori-Fossi, B. C. 1996, ApJS, 106, 143
Brosius, J. W., Thomas, R. J., Davila, J. M., & Landi, E. 2000, ApJ, 543, 1016
Brueckner, G. E., & Bartoe, J.-D. F. 1983, ApJ, 272, 329
Cairns, I. H., & Robinson, R. D. 1987, Sol. Phys., 111, 365
Cane, H. V., Stone, R. G., Fainberg, J., et al. 1981, GRL, 8, 1285
Chen, P. F., Wu, S. T., Shibata, K., & Fang, C. 2002, ApJ, 572, L99
Close, R. M., Parnell, C. E., Mackay, D. H., & Priest, E. R. 2003, Sol. Phys., 212, 251
Cook, J. W., Keenan, F. P., Harra, L. K., & Tayal, S. S. 1994, ApJ, 429, 924
Del Zanna, G., & Mason, H. E. 2003, A&A, 406, 1089
Dere, K. P. 1996, ApJ, 472, 864
Forsyth, R. J., Balogh, A., Horbury, T. S., et al. 1996, A&A, 316, 287
Gallagher, P. T., Mathioudakis, M., Keenan, F. P., et al. 1999, ApJ, 524, L133
Gallagher, P. T., Phillips, K. J. H., Lee, J., et al. 2001, ApJ, 558, 411
Gary, G. A. 2001, Sol. Phys., 203, 71
Harrison, R. 1986, A&A, 162, 283
Hudson, H. S., Khan, J. I., Lemen, J. R., Nitta, N. V., & Uchida, Y. 2003, Sol. Phys., 212, 121
Kahler, S. 1994, ApJ, 428, 837
Klassen, A., Aurass, H., Klein, K.-L., Hofmann, A., & Mann, G. 1999, A&A, 343, 287
Klassen, A., Aurass, H., Mann, G., & Thompson, B. J. 2000, A&AS, 141, 357
Koutchmy, S. 1994, Adv. Space Res., 14, 4, 29
Krucker, S., Larson, D. E., Lin, R. P., & Thompson, B. J. 1999, ApJ, 519, 864
Landi, E., & Landini, M. 1998, A&A, 340, 265
Li, J., Raymond, C., Acton, L. W., et al. 1998, ApJ, 506, 431
Lin, H., Kuhn, J. R., & Coulter, R. 2004, ApJ, 613, L177
Lites, B. W., & Socas-Navarro, H. 2004, ApJ, 613, 600
Mann, G. 1995, J. Plasma Phys., 53, 109
Mann, G. 1997, in Planetary Radio Emissions IV, ed. H. O. Rucker, S. J. Bauer, & A. Lecacheux (Vienna: Austrian Academy of Sciences), 395
Mann, G., & Lühr, H. 1994, ApJS, 90, 577
Mann, G., & Classen, H.-T. 1995, A&A, 304, 576
Mann, G., & Klassen, A. 2002, in Proc. 10th European Solar Physics Meeting, ed. A. Wilson, ESA SP-506, 1, 245
Mann, G., Aurass, H., Klassen, A., Estel, C., & Thompson, B. J. 1999a, in Proc. 8th SOHO Workshop, ed. B. Kaldeich-Schürmann, ESA SP-446, 477
Mann, G., Jansen, F., MacDowall, R. J., Kaiser, M. L., & Stone, R. G. 1999b, A&A, 348, 614
Mann, G., Klassen, A., Aurass, H., & Classen, H.-T. 2003, A&A, 400, 329
Mason, H. E., Landi, E., Pike, C. D., & Young, P. R. 1999, Sol. Phys., 189, 129
Moreton, G. E., & Ramsey, H. E. 1960, PASP, 72, 357
Moses, D., Clette, F., Delaboudinière, J.-P., et al. 1997, Sol. Phys., 175, 571
Narukage, N., Hudson, H. S., Morimoto, T., et al. 2002, ApJ, 572, L109
Newkirk, G. A. 1961, ApJ, 133, 983
O'Shea, E., Doyle, J. G., & Keenan, F. P. 1998, A&A, 338, 1102
Parenti, S., Bromage, B. J. I., Poletto, G., et al. 2000, A&A, 363, 800
Pauluhn, A., & Solanki, S. K. 2003, A&A, 407, 359
Pevtsov, A. A., & Acton, L. W. 2001, ApJ, 554, 416
Priest, E. R. 1982, Solar Magnetohydrodynamics (Dordrecht: Reidel)
Rabin, D. M., DeVore, C. R., Sheely, N. R., Jr., et al. 1991, in Solar Interior and Atmosphere, ed. A. N. Cox, W. C. Livingston, & M. S. Matthews (Tucson: Univ. Arizona Press), 781
Reames, D. V., Barbier, L. M., & Ng, C. K. 1996, ApJ, 466, 473
Saito, K. 1970, Ann. Tokyo Astr. Obs., 12, 53
Scherrer, P. H., Bogart, R. S., Bush, R. I., et al. 1995, Sol. Phys., 162, 129
Schrijver, C. J., Title, A. M., Van Ballegooijen, A. A., Hagenaar, H. J., & Shine, R. A. 1997, ApJ, 487, 424
Smerd, S. F., Sheridan, K. V., & Stewart, R. T. 1974, in IAU Symp. 57, ed. G. A. Newkirk, 389
Smith, E. J., & Balogh, A. 1995, GRL, 22, 3317
Smith, C. W., Acuna, M. H., Burlaga, L. F., et al. 1998, Space Sci. Rev., 86, 613
Stewart, R. T., McCabe, M., Koomen, M. J., Hansen, F., & Dulk, G. 1974a, Sol. Phys., 26, 203
Stewart, R. T., Howard, R. A., Hansen, F., Gergely, T., & Kundu, M. R. 1974b, Sol. Phys., 36, 219
Thompson, B. J., Plunkett, S. P., Gurman, J. B., et al. 1998, Geophys. Res. Lett., 25, 2465
Uchida, Y. 1960, PASJ, 12, 676
Uchida, Y. 1968, Sol. Phys., 4, 30
Uchida, Y., Altschuler, M. D., & Newkirk, G., Jr. 1973, Sol. Phys., 28, 495
Vainio, R., & Khan, J. I. 2004, ApJ, 600, 451
Vršnak, B., & Lulić., S. 2000, Sol. Phys., 196, 157
Vršnak, B., Ruždjak, V., Zlobec, P., & Aurass, H. 1995, Sol. Phys., 158, 331
Vršnak, B., Warmuth, A., Brajša, R., & Hanslmeier, A. 2002a, A&A, 394, 299
Vršnak, B., Magdalenić, J., Aurass, H., & Mann, G. 2002b, A&A, 396, 673
Wagner, W. J., & MacQueen, R. M. 1983, A&A, 120, 136
Wang, Y.-M. 2000, ApJ, 543, L89
Warmuth, A., Vršnak, B., Aurass, H., & Hanslmeier, A. 2001, ApJ, 560, L105
Warmuth, A., Vršnak, B., Magdalenić, J., Hanslmeier, A., & Otruba, W. 2004a, A&A, 418, 1101
Warmuth, A., Vršnak, B., Magdalenić, J., Hanslmeier, A., & Otruba, W. 2004b, A&A, 418, 1117
Warren, H. P. 1999, Sol. Phys., 190, 363
Warren, H. P., & Warshall, A. D. 2002, ApJ, 571, 999
Warren, H. P., & Winebarger, A. R. 2003, ApJ, 596, L113
Wild, J. P., & McCready, L. L. 1950, Aust. J. Sci. Res. A, 3, 387
Wu, S. T., Zheng, H., Wang, S., et al. 2001, J. Geophys. Res., 106, 25089
Zhao, J., Kosovichev, A. G., & Duvall, T. L., Jr. 2001, ApJ, 557, 384